Synthesis and Magnetic Properties of 12L-Perovskites

$Ba_4LnIr_3O_{12}$ (Ln = Lanthanides)

Yuki Shimoda, Yoshihiro Doi, Makoto Wakeshima and Yukio Hinatsu

Division of Chemistry, Hokkaido University, Sapporo 060-0810, Japan

Abstract

New quadruple perovskite oxides $Ba_4LnIr_3O_{12}$ (Ln = lanthanides) were prepared and their magnetic properties were investigated. They crystallize in the monoclinic 12L-perovskite-type structure with space group C2/m. The Ir_3O_{12} trimers and LnO_6 octahedra are alternately linked by corner-sharing and form the perovskite-type structure with 12 layers. The Ln and Ir ions are both in the tetravalent state for Ln = Ce, Pr, and Tb compounds ($Ba_4Ln^{4+}Ir^{4+}{}_3O_{12}$), and for other compounds (Ln = La, Nd, Sm-Gd, Dy-Lu), Ln ions are in the trivalent state and the mean oxidation state of Ir ions is +4.33 ($Ba_4Ln^{3+}Ir^{4.33+}{}_3O_{12}$). An antiferromagnetic transition has been observed for Ln = Ce, Pr, and Tb compounds at 10.5, 35, and 16 K, respectively, while the other compounds are paramagnetic down to 1.8 K.

1. Introduction

The perovskite oxides ABO_3 form a wide family of compounds, reflecting the flexibility in the chemical composition and crystal structure. Structures of perovskite compounds can be regarded as the stacking of close-packed AO_3 layers and the filling of subsequent octahedral sites by B-site ions. The difference in the stacking sequence changes the way of linkage of BO_6 octahedra: the corner-sharing BO_6 in the cubic perovskite (3L: three-layer) with *abc*… sequence, the face-sharing BO_6 in 2L-perovskite (2L: two-layer) with *ab*… sequence, and mixed linkages between the corner- and face-sharing in various intergrowth structures [1].

The 6L-perovskites $Ba_3MM'_2O_9$ (M = alkali metals, alkaline earth elements, 3d transition metals, lanthanides; M' = Ru, Ir) have been investigated [2-29]. In this structure, two $M'O_6$ octahedra are connected by face-sharing and form an M'_2O_9 dimer. These dimers and MO_6 octahedra are placed alternately; thus, 6-layer (6L) structure is generated. The stacking sequence of AO_3 layers is *abacbc*.... For many of these compounds, an antiferromagnetic spin-pairing occurs in the M'_2O_9 dimer even at room temperature. In addition, the $Ba_3MM'_2O_9$ compounds show magnetic transitions at low temperatures, which originates from the magnetic interaction between M and M' ions.

Then, we focused our attention on new quadruple perovskite compounds $Ba_4LnRu_3O_{12}$ (Ln = lanthanides) in which the ratio of Ln:Ru is 1:3. In the $Ba_4LnRu_3O_{12}$, three RuO_6 octahedra are face-shared, forming a Ru_3O_{12} trimer, and we thought that peculiar magnetic behavior due to new alignment of the Ln and Ru ions should be observed [30]. In the $Ba_3LnRu_2O_9$, the ground state of the total spin of the isolated Ru_2O_9 dimer may be zero, i.e., $S_{total} = S_1 + S_2 = 0$, for the case that the antiferromagnetic coupling exists between the Ru ions. On the other hand, in the case of $Ba_4LnRu_3O_{12}$ compounds, the total magnetic moment of the Ru_3O_{12} trimer does not disappear as far as three Ru ions are equivalent. The results of the magnetic susceptibility and specific heat measurements are that although no long-range magnetic ordering of Ru^{4+} ions was

found for the 6L-perovskite $Ba_3TbRu_2O_9$, $Ba_4TbRu_3O_{12}$ showed an antiferromagnetic transition at 24 K, which is due to the relatively strong magnetic interaction between Tb^{4+} ions and Ru_3O_{12} trimer via the Tb–O–Ru pathway owing to an uncancelled magnetic moment in the Ru_3O_{12} trimer.

In this work, we challenged preparing new iridium-containing quadruple perovskite compounds $Ba_4LnIr_3O_{12}$. Battle et al. reported that the compounds $Ba_4MIr_3O_{12}$ (M = Li, Na, Mg, Y, Lu, Zr, and Ce) adopted the 6L-perovskite structure, i.e., the face-sharing octahedral were occupied solely by Ir atoms, and the corner-sharing octahedral were occupied statistically by the remaining Ir and the M atoms in a 1:3 ratio [31]. Although these M atoms have different charges and sizes, all the $Ba_4MIr_3O_{12}$ compounds had the same crystal structure. We could introduce the Ir atoms in a 3:1 ratio with lanthanides into the B-site of the perovskite, and stabilize the fully ordered 12L perovskite structure. In order to elucidate the properties of Ir_3O_{12} trimer, the magnetic properties of these $Ba_4LnIr_3O_{12}$ compounds were investigated.

2. Experimental

2.1. Synthesis

Polycrystalline samples of $Ba_4LnIr_3O_{12}$ (Ln = La–Nd, Sm–Lu) were prepared by the standard solid-state reaction. $BaIrO_3$, $BaLnO_3$ (Ln = Ce, Pr, Tb), BaO, BaO_2, and Ln_2O_3 (Ln = La, Pr, Sm-Gd, Dy-Lu) were used as starting materials. Among them, La_2O_3 and Nd_2O_3 absorb moistures in air and easily form lanthanide hydroxides $Ln(OH)_3$. Then, these oxides were heated at 900 °C for 12 h so as to decompose into Ln_2O_3 before use. It is known that both the ternary oxides $BaIrO_3$ and $BaLnO_3$ are formed with stoichiometric compositions. $BaIrO_3$ was prepared by the solid state reaction of $BaCO_3$ and IrO_2 at 900 °C for 12 h and at 1100 °C for 12 h [32, 33]. $BaLnO_3$ (Ln = Ce, Pr, Tb) were obtained by heating mixtures of $BaCO_3$ and CeO_2 (or Pr_6O_{11}, Tb_4O_7) in an oxygen flowing atmosphere [34-36]. These starting materials were weighed out in the appropriate metal ratio, and well mixed in an agate mortar. The mixtures were pressed

into pellets and enclosed with platinum tubes, and they were sealed in evacuated silica tubes. Then, they were fired at 1250 °C for 36 h.

The obtained phases were identified by powder X-ray diffraction (XRD) measurements. Impurity phases such as 6L-perovskite $Ba_3LnIr_2O_9$ [25, 26] were formed due to the sublimation of Ba oxides and Ir oxides. In order to decrease such impurity phases, the excess amount (~ 30 %) of $BaIrO_3$ [32, 33] was added during sample preparation.

2.2. X-ray diffraction analysis

Powder X-ray diffraction profiles were measured using a Rigaku Multi-Flex diffractometer with Cu-Kα radiation equipped with a curved graphite monochromator. The data were collected by step-scanning in the angle range of $10° \leq 2\theta \leq 120°$ at a 2θ step-size of 0.02°. The X-ray diffraction data were analyzed by the Rietveld technique, using the programs RIETAN2000 [37].

2.3. Magnetic susceptibility measurements

The temperature-dependence of the magnetic susceptibility was measured in an applied field of 0.1 T over the temperature range of $1.8\ \text{K} \leq T \leq 400\ \text{K}$, using a SQUID magnetometer (Quantum Design, MPMS5S). The susceptibility measurements were performed under both zero-field-cooled (ZFC) and field-cooled (FC) conditions. The former was measured upon heating the sample to 400 K under the applied magnetic field of 0.1 T after zero-field cooling to 1.8 K. The latter was measured upon cooling the sample from 400 to 1.8 K at 0.1 T.

2.4. Specific heat measurements

Specific heat measurements were performed using a relaxation technique by a commercial heat capacity measuring system (Quantum Design, PPMS) in the temperature range of 1.8-400 K. The sintered sample in the form of a pellet was mounted on a thin alumina plate with Apiezon grease for better thermal contact.

3. Results and Discussion

3.1. Synthesis and analysis of the structure

We succeeded in synthesizing new perovskite-related compounds $Ba_4LnIr_3O_{12}$ (Ln = La–Nd, Sm–Lu). Figure 1 shows the powder X-ray diffraction profile of $Ba_4NdIr_3O_{12}$ as an example. To analyze the XRD diffraction profile, we used the crystal structure data of $Ba_4LnRu_3O_{12}$ as the initial structural model. The $Ba_4LnRu_3O_{12}$ for Ln = Tb-Lu have a hexagonal unit cell with space group *R*-3*m* (No.166), while those for Ln = La-Nd, Sm-Gd have a monoclinic unit cell with space group *C*2/*m* (No.12) [30]. In the case that the space group *R*-3*m* were applied, the X-ray diffraction lines observed at 2θ = 27˚ and 30˚, for example, should not be split. However, experimental results show that each of these diffraction lines is split into two diffraction lines, as shown in the inset of Fig. 1. All the $Ba_4LnIr_3O_{12}$ compounds prepared in this study were indexed with a monoclinic 12L-perovskite type cell with space group *C*2/*m*.

Figure 2 shows the crystal structure of $Ba_4LnIr_3O_{12}$. Three IrO_6 octahedra are connected to each other by face-sharing and form an Ir_3O_{12} trimer. The Ir_3O_{12} trimers and LnO_6 octahedra are alternately linked by corner-sharing. As shown in this figure, perovskite-type structure with 12 layers is formed (the stacking sequence: *ababcacabcbc*...). Similar structures have been reported for $Ba_4ZrRu_3O_{12}$ [38] and $Ba_4LnMn_3O_{12}$ (Ln = Ce, Pr) [39]. The distances between Ir atoms in the Ir_3O_{12} trimer are determined to be 2.48~2.60 Å, which are much shorter than double the metallic radius of Ir (2.72 Å) [40]. This means that a strong interaction between Ir ions should exist in the trimer. The oxidation state of Ln and Ir are both tetravalent for Ln = Ce, Pr, Tb compounds ($Ba_4Ln^{4+}Ir^{4+}{}_3O_{12}$), and Ln ions are in the trivalent state and the mean oxidation state of Ir ions is +4.33 for other compounds ($Ba_4Ln^{3+}Ir^{4.33+}{}_3O_{12}$).

Figure 3 shows the variation of lattice parameters with the ionic radius of Ln^{3+}. Except for the compounds having the Ln^{4+} ion (Ln = Ce, Pr, and Tb), the lattice parameters *a*, *b*, and *c* monotonously increase with the Ln^{3+} ionic radius. The angle β increases from 90˚ with the Ln^{3+} ionic radius, which indicates that with increasing the size of the Ln^{3+} ion, the crystal structures

of $Ba_4LnIr_3O_{12}$ are more distorted because of the larger difference in the ionic radius between Ln and Ir ions.

3.2. Magnetic properties

3.2.1. $Ba_4Ln^{3+}Ir^{4.33+}{}_3O_{12}$ (Ln = La, Nd-Gd, Dy-Lu)

Figures 4 (a) and (b) show the temperature dependence of the reciprocal magnetic susceptibility for $Ba_4LnIr_3O_{12}$ (Ln = La, Nd-Gd, Dy-Lu). These compounds are paramagnetic down to 1.8 K. In the temperature range where the Curie-Weiss law holds, the effective magnetic moments were determined and they are listed in Table 1. The effective magnetic moments determined for $Ba_4LnIr_3O_{12}$ (μ_{eff}) are close to the magnetic moments of Ln^{3+} ions (μ_{Ln}), i.e., the contribution of the trimer $Ir^{4.33+}{}_3O_{12}$ to the magnetic properties of $Ba_4LnIr_3O_{12}$ is negligible. This result can be understood in the following.

The distances between Ir atoms in the Ir_3O_{12} trimer are 2.48~2.60 Å. The short Ir-Ir interatomic distances in the Ir_3O_{12} trimer suggest the overlap of metal d orbitals having lobes along the threefold symmetry axis, which means the formation of molecular orbitals in the Ir_3O_{12} trimer. The electronic structure of Ru_3Cl_{12} with D_{3d} point symmetry has been described [41]. The energy scheme of Ir_3O_{12} in the $Ba_4LnIr_3O_{12}$ should be similar to the case of Ru_3Cl_{12}, but the degenerated energy levels are expected to be split into more levels due to the monoclinic distortion of the Ir_3O_{12} trimer and to the spin-orbit coupling of the 5d electrons (Ir ions). The electronic configuration of the $Ir^{4.33+}{}_3O_{12}$ trimer (the number of 5*d* electrons is 14) with D_{3d} point symmetry is $(a_{1g})^2(e_g)^4(a_{2u})^2(e_u)^4(e_g)^2$. Figure 5 illustrates the schematic energy level diagrams for the Ir-Ir interactions in (a) $Ir^{4.33+}{}_3O_{12}$ and (b) $Ir^{4+}{}_3O_{12}$. The highest occupied e_g orbital of the Ir_3O_{12} trimer should be split into two singlets by the monoclinic distortion, which causes the S = 0 ground state of the filled HOMO level. Therefore, the $Ir^{4.33+}{}_3O_{12}$ trimer does not contribute to the magnetic properties of $Ba_4LnIr_3O_{12}$ (Ln = La, Nd-Gd, Dy-Lu), and both $Ba_4LaIr_3O_{12}$ and $Ba_4LuIr_3O_{12}$ are diamagnetic.

3.2.2. $Ba_4Ln^{4+}Ir^{4+}{}_3O_{12}$ (Ln = Ce, Pr, Tb)

The temperature dependence of the magnetic susceptibility and the reciprocal susceptibility for $Ba_4CeIr_3O_{12}$ is shown in Figs. 6 (a) and (b), respectively. The same temperature dependence of the susceptibility and the reciprocal susceptibility for $Ba_4PrIr_3O_{12}$ and $Ba_4TbIr_3O_{12}$ is depicted in Figs. 7 and 9, respectively. From the Curie-Weiss fitting in the temperature range between 300 and 400 K, the effective magnetic moments of $Ba_4LnIr_3O_{12}$ with Ln = Ce, Pr, and Tb are obtained to be 1.24, 2.94, and 8.02 μ_B, respectively (Table 1). When the magnetic ions in these compounds are magnetically independent, the effective magnetic moments of $Ba_4LnIr_3O_{12}$ should be calculated from the equation $\mu_{cal} = \sqrt{\mu_{Ln^{4+}}{}^2 + 3 \times \mu_{Ir^{4+}}{}^2}$. However, the effective magnetic moments obtained experimentally are far below the calculated moments. We will discuss the magnetic behavior of $Ir^{4+}{}_3O_{12}$ trimer in the same way as the case of $Ir^{4.33+}{}_3O_{12}$. The $Ir^{4+}{}_3O_{12}$ trimer has fifteen 5*d* electrons, and its electronic configuration is $(a_{1g})^2(e_g)^4(a_{2u})^2(e_u)^4(e_g)^3$, which should cause the S = 1/2 ground state (see Fig. 5 (b)). In this case, the effective magnetic moments for $Ba_4Ln^{4+}Ir^{4+}{}_3O_{12}$ (Ln = Ce, Pr, Tb) are calculated from the equation $\mu_{cal} = \sqrt{\mu_{Ln^{4+}}{}^2 + \mu_{S=1/2}{}^2}$, and they are listed in Table 1. The effective magnetic moments of $Ba_4LnIr_3O_{12}$ experimentally determined are almost in accordance with the calculated moments. The moment of $Ba_4CeIr_3O_{12}$ is a little smaller than the expected value, which is due to existence of impurities such as $Ba_3CeIr_2O_9$. The $Ba_3CeIr_2O_9$ shows a very small effective magnetic moment, because the magnetic moments of Ir ions cancel each other in the Ir_2O_9 dimer [25]. In the following, magnetic properties of each $Ba_4LnIr_3O_{12}$ (Ln = Ce, Pr, Tb) compound at lower temperatures will be described.

3.2.2.1. $Ba_4CeIr_3O_{12}$

Magnetic susceptibility measurements on $Ba_4CeIr_3O_{12}$ show that an antiferromagnetic transition occurs at 10.5 K (see Fig. 6 (a)). On the other hand, ruthenium-containing compound $Ba_4CeRu_3O_{12}$ is paramagnetic down to 1.8 K [30]. Since the tetravalent cerium ion is

diamagnetic, the S = 1/2 state of the $Ir^{4+}{}_3O_{12}$ trimer is responsible for the antiferromagnetic transition of $Ba_4CeIr_3O_{12}$. Specific heat measurements on $Ba_4CeIr_3O_{12}$ also show a clear anomaly against temperature at 10.5 K, indicating the occurrence of the long-range antiferromagnetic ordering at this temperature. Below 5 K, the magnetic susceptibility of $Ba_4CeIr_3O_{12}$ increases with decreasing temperature, which is probably due to the existence of small amount of paramagnetic impurities such as $Ba_3CeIr_2O_9$. The $Ba_3CeIr_2O_9$ is paramagnetic down to 1.8 K [25].

3.2.2.2. $Ba_4PrIr_3O_{12}$

The results of the magnetic susceptibility measurements (Fig. 7 (a)) show that $Ba_4PrIr_3O_{12}$ orders antiferromagnetically at 35 K. Its transition temperature is higher than that of $Ba_4CeIr_3O_{12}$. This reflects the fact that the Pr^{4+} ion contributes to the magnetic superexchange interaction between Ir^{4+} ions. This compound also shows the increase of magnetic susceptibility with decreasing temperature below 10 K. This behavior is ascribed to the paramagnetic impurities such as $Ba_3PrIr_2O_9$, which is paramagnetic down to 1.8 K [25].

In order to obtain detailed information about the low-temperature magnetic ordering, specific heat measurements were performed down to 1.8 K. Figure 8 (a) shows the temperature dependence of the specific heat (C_p) divided by temperature (C_p/T) for $Ba_4PrIr_3O_{12}$. A specific heat anomaly has been observed at 35 K, which corresponds to the results by magnetic susceptibility measurements. This result indicates that the long range antiferromagnetic ordering occur at this temperature. To evaluate the magnetic contribution to the specific heat (C_{mag}), we have to subtract the contribution of lattice specific heat (C_{lat}) from the total specific heat ($C_{mag} = C_p - C_{lat}$). The lattice specific heat was estimated by using the specific heat data of a diamagnetic compound $Ba_4LuIr_3O_{12}$ (the dotted line of Fig. 8 (a)). Figure 8 (b) shows the temperature dependence of the magnetic specific heat divided by temperature (C_{mag}/T). The magnetic entropy change due to the magnetic ordering of $Ba_4PrIr_3O_{12}$ (S_{mag}) is calculated by the relation $S_{mag} = \int (C_{mag}/T) dT$. Its temperature dependence is also shown in Fig. 8 (b). The total

magnetic entropy change is obtained to be 8.7 J/mol K.

The corresponding ruthenium-containing compound $Ba_4PrRu_3O_{12}$ shows an antiferromagnetic transition at 2.4 K, and its specific heat measurements indicated that the antiferromagnetic ordering is only due to the ground Kramers doublet of Pr^{4+} ion [30]. The crystal structure of $Ba_4PrIr_3O_4$ is the same with that of $Ba_4PrRu_3O_4$. In a similar way, the ground Kramers doublet of Pr^{4+} ion in a low symmetric crystal field is responsible for the antiferromagnetic ordering of $Ba_4PrIr_3O_4$. Therefore, its contribution to the magnetic entropy change is estimated to be Rln2. The magnetic entropy change due to the antiferromagnetic ordering of the $Ir^{4+}{}_3O_{12}$ trimer (S = 1/2) is also calculated to be Rln2. Although the magnetic entropy change obtained experimentally (S_{mag} = ~ 8.7 J/mol K) is a little smaller than that calculated 2 Rln2 (= 11.52 J/mol K), we can conclude that both the 4f electron of Pr^{4+} and the 5d electron of Ir^{4+} contribute to the antiferromagnetic ordering of $Ba_4PrIr_3O_4$.

3.2.2.3. $Ba_4TbIr_3O_{12}$

Figure 9 (a) shows that $Ba_4TbIr_3O_{12}$ orders antiferromagnetically at 16 K. Below this temperature, the divergence between the ZFC and FC susceptibilities is observed, which indicates a small ferromagnetic moment. For compounds with low crystal symmetry such as monoclinic, a Dzyaloshinsky-Moriya (D-M) interaction can exist between the ordered magnetic moments, which results in the existence of a weak ferromagnetic moment associated with the antiferromagnetism. The increase of magnetic susceptibility with decreasing temperature below 5 K is probably due to the paramagnetic impurities such as $Ba_3TbIr_2O_9$ and Ba_2TbIrO_6 [25, 42]. Figure 10 (a) shows the temperature dependence of the specific heat divided by temperature (C_p/T) for $Ba_4TbIr_3O_{12}$. A clear λ-type specific heat anomaly has been observed at 16 K, which indicates that the long range antiferromagnetic ordering occurs at this temperature. In the same way as the case for $Ba_4PrIr_3O_{12}$, the magnetic specific heat (C_{mag}) was evaluated by subtracting the specific heat of $Ba_4LuIr_3O_{12}$ (C_{lat}) from the total specific heat ($C_{mag} = C_p - C_{lat}$). Figure 10 (b) shows the temperature dependence of the magnetic specific heat divided temperature

(C_{mag}/T). The magnetic entropy change for $Ba_4TbIr_3O_{12}$ (S_{mag}) is also shown in the same figure, and it is obtained to be ~ 18.5 J/mol K. Magnetic entropy change due to the magnetic ordering of Tb^{4+} (the electronic configuration of Tb^{4+}: $[Xe]f^7$; the S = 7/2 ground state) is $R\ln(2S+1)$ = 17.3 J/mol K. The experimental value is larger than this value, which indicates the contribution of the $Ir^{4+}{}_3O_{12}$ trimer (S = 1/2) to the magnetic ordering at 16K. However, the experimental value is below the estimated total magnetic entropy change (23.1 J/mol K). The reason for this may be that the magnetic entropy is partially lost at higher temperatures because of the short range ordering. Similar smaller magnetic entropy change was reported for $Ba_4TbRu_3O_{12}$, i.e., the magnetic entropy change due to the magnetic ordering of Tb^{4+} was 12.5 J/mol K [30].

Summary

New quadruple perovskites $Ba_4LnIr_3O_{12}$ were prepared and they form the perovskite-type structure with 12 layers, in which Ir_3O_{12} trimers and LnO_6 octahedra are alternately linked by corner-sharing. For Ln = Ce, Pr, and Tb compounds, an antiferromagnetic transition was observed at low temperatures, while the other compounds are paramagnetic down to 1.8 K.

Acknowledgement

This work was supported by Grant-in-aid from the Ministry of Education, Science, Sports, and Culture of Japan.

References

[1] J. M. Longo and J. A. Kafalas, *J. Solid State Chem.*, **1**, 103−108 (1969).

[2] R. C. Bryne and C. W. Moeller, *J. Solid State Chem.*, **2**, 228−235 (1970).

[3] J. Darriet, M. Drillon, G. Villeneuve, and P. Hagenmuller, *J. Solid State Chem.*, **19**, 213−220 (1976).

[4] H.-U. Schaller and S. Kemmler-Sack, *Z. Anorg. Allg. Chem.*, **473**, 178-188 (1981).

[5] I. Thumm, U. Treiber, and S. Kemmler-Sack, *Z. Anorg. Allg. Chem.*, **477**, 161-166 (1981).

[6] U. Treiber, S. Kemmler-Sack, A. Ehmann, H.-U. Schaller, E. Dürrschmidt, I. Thumm and H. Bader, *Z. Anorg. Allg. Chem.*, **481**, 143-152 (1981).

[7] H. W. Zandbergen and D. J. W. IJdo, *Acta Crystallogr.*, C**40**, 919-922 (1984).

[8] D. Verdoes, H. W. Zandbergen, and D. J. W. IJdo, *Acta Crystallogr.*, C**41**, 170-173 (1985).

[9] P. Lightfoot and P. D. Battle, *J. Solid State Chem.*, **89**, 174−183 (1990).

[10] P. D. Battle, S. H. Kim, and A. V. Powell, *J. Solid State Chem*., **101**, 161-172 (1992).

[11] D. Schluter and H.-K. Müller-Buschbaum, *J. Alloys Compd.*, **190**, L43-L44 (1993).

[12] S. Scheske and H.-K. Müller-Buschbaum, *J. Alloys Compd.*, **198**, 173-176 (1993).

[13] M. Rath and H.-K. Müller-Buschbaum, *J. Alloys Compd.*, **210**, 119-123 (1994).

[14] S. H. Kim and P. D. Battle, *J. Solid State Chem*., **114**, 174-183 (1995).

[15] P. D. Battle, J. G. Gore, R. C. Hollyman, and A. V. Powell, *J. Alloys Compd.*, **218**, 110-116 (1995).

[16] D.-K. Jung, G. Demazeau, J. Etourneau, and M. A. Subramanian, *Mater. Research Bull*., **30**, 113-123 (1995).

[17] J. T. Rijssenbeek, P. Matl, B. Batlogg, N. P. Ong, and R. J. Cava, *Phys.Rev.*, **58**, 10315−10318 (1998).

[18] J. T. Rijssenbeek, Q. Huang, R. W. Erwin, H. W. Zandbergen, and R. J. Cava, *J. Solid*

State Chem., **146**, 65−72 (1999).

[19] Y. Doi, Y. Hinatsu, Y. Shimojo, and Y. Ishii, *J. Solid State Chem*., **161**, 113-120 (2001).

[20] Y. Doi, M. Wakeshima, Y. Hinatsu, A. Tobo, K. Ohoyama, and Y. Yamaguchi, *J. Mater. Chem*., **11**, 3135–3140 (2001).

[21] K.E. Stitzer, M. D. Smith, W. R. Gemmill, and H.-C. zur Loye*, J. Amer. Chem.Soc.*, **124**, 13877–13885 (2002).

[22] Y. Doi, K. Matsuhira, and Y. Hinatsu, *J. Solid State Chem.*, **165**, 317-323 (2002).

[23] Y. Doi and Y. Hinatsu, *J. Mater. Chem.*, **12**, 1792-1795 (2002).

[24] E. Quarez, M. Huve, F. Abraham, and O. Mentre, *Solid State Sciences*, **5**, 951-963 (2003).

[25] Y. Doi and Y. Hinatsu, *J. Phys.: Condens. Matter*., **16**, 2849–2860 (2004).

[26] Y. Doi and Y. Hinatsu, *J. Solid State Chem.*, **177**, 3239-3244 (2004).

[27] M. W. Lufaso and H.-C. zur Loye*, Inorg. Chem.*, **44**, 9143–9153 (2005).

[28] M. W. Lufaso and H.-C. zur Loye*, Inorg. Chem.*, **44**, 9154–9161 (2005).

[29] T. Sakamoto, Y. Doi, and Y. Hinatsu, *J. Solid State Chem.*, **179**, 2595-2601 (2006).

[30] Y. Shimoda, Y. Doi, Y. Hinatsu, and K. Ohoyama, *Chem Mater.*, **20**, 4512-4518 (2008).

[31] J. G. Gove and P. D. Battle, *J. Mater. Chem.*, **6**, 201-206 (1996).

[32] P.C. Donohue, L. Katz and R. Ward, *Inorg. Chem.*, **4**, 306–310 (1965).

[33] T. Siegrist, B. L. Chamberland, *J. Less-Common Metals*, **170**, 93-99 (1991).

[34] Y. Hinatsu and N. Edelstein, *J. Alloys Compd.*, **250**, 400-404 (1997).

[35] M. Itoh and Y. Hinatsu, *J. Alloys Compd.*, **264**, 119-124 (1998).

[36] K. Tezuka, Y. Hinatsu, Y. Shimojo, and Y. Morii, *J. Phys.: Condens. Matter*., **10**, 11703–11712 (1998).

[37] F. Izumi and T. Ikeda, *Mater. Sci. Forum*, **321–324**, 198–203 (2000).

[38] C. H. De Vreugd, H. W. Zandbergen, and D. J. W. IJdo, *Acta Crystallogr*., C**40**, 1987-1989 (1984).

[39] A. F. Fuentes, K. Boulahya, and U. Amador, *J. Solid State Chem*., **177**, 714-720 (2004).

[40] A. F. Wells, *Structural inorganic chemistry 5th Ed.*, Oxford Clarendon Press., (1984).

[41] B. E. Bursten, F. A. Cotton, and A. Fang, *Inorg. Chem.*, **22**, 2127-2133 (1983).

[42] M. Wakeshima, D. Harada, and Y. Hinatsu, *J. Mater. Chem*., **10**, 419–422 (2000).

Figure captions

Fig. 1 X-ray diffraction profiles of $Ba_4NdIr_3O_{12}$. The calculated and observed profiles are shown on the top solid line and cross markers, respectively. The vertical marks in the middle show positions calculated for Bragg reflections. The lower trace is a plot of the difference between calculated and observed intensities. The inset shows the profiles between $25^\circ \leq 2\theta \leq 32^\circ$. The diffraction lines are indexed with a monoclinic 12L-perovskite type cell.

Fig. 2 The schematic crystal structure of $Ba_4LnIr_3O_{12}$.

Fig. 3 The variation of lattice parameters for $Ba_4LnIr_3O_{12}$ against the ionic radius of Ln^{3+}.

Fig. 4 (a) Temperature dependence of the reciprocal magnetic susceptibilities for $Ba_4LnIr_3O_{12}$ (Ln = Nd, Tm, Yb). The solid line is the Curie-Weiss fitting.

(b) Temperature dependence of the magnetic susceptibilities for $Ba_4LnIr_3O_{12}$ (Ln = Gd, Dy-Er). The solid line is the Curie-Weiss fitting.

Fig. 5 Schematic energy level diagrams for (a) $Ir^{4.33+}{}_3O_{12}$ trimer and (b) $Ir^{4+}{}_3O_{12}$ trimer.

Fig. 6 (a) Temperature dependence of the magnetic susceptibilities for $Ba_4CeIr_3O_{12}$. The inset shows the magnetic susceptibilities at low temperatures.

(b) The reciprocal magnetic susceptibility against temperature. The solid line is the Curie-Weiss fitting.

Fig. 7 (a) Temperature dependence of the magnetic susceptibilities for $Ba_4PrIr_3O_{12}$. The inset shows the magnetic susceptibilities at low temperatures.

(b) The reciprocal magnetic susceptibility against temperature. The solid line is the Curie-Weiss fitting.

Fig. 8 Temperature dependence of (a) the specific heat divided by temperature (C_p/T) and (b) the magnetic specific heat divided by temperature (C_{mag}/T) and the magnetic entropy (S_{mag}) for $Ba_4PrIr_3O_{12}$.

Fig. 9 (a) Temperature dependence of the magnetic susceptibilities for $Ba_4TbIr_3O_{12}$. The

inset shows the magnetic susceptibilities at low temperatures.

(b) The reciprocal magnetic susceptibility against temperature. The solid line is the Curie-Weiss fitting.

Fig. 10 Temperature dependence of (a) the specific heat divided by temperature (C_p/T) and (b) the magnetic specific heat divided by temperature (C_{mag}/T) and the magnetic entropy (S_{mag}) for $Ba_4TbIr_3O_{12}$.

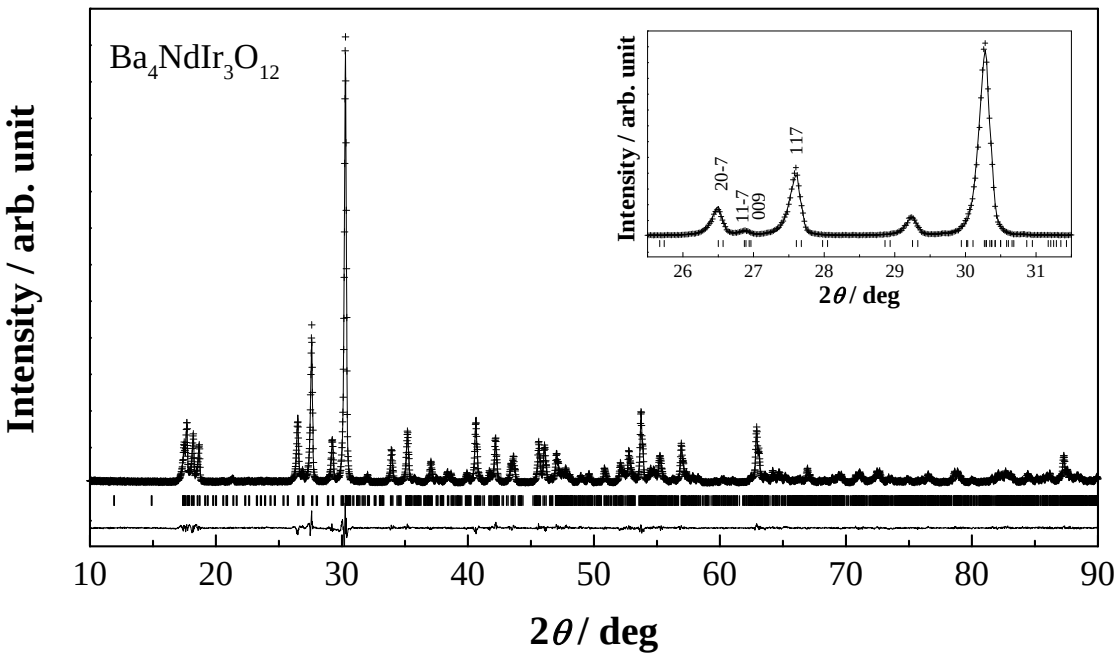
Ba4NdIr3O12
Intensity / arb. unit
2θ / deg
10
20
30
40
50
60
70
80
90
Intensity / arb. unit
20-7
11-7
009
117
26
27
28
29
30
31
2θ / deg

Fig. 1

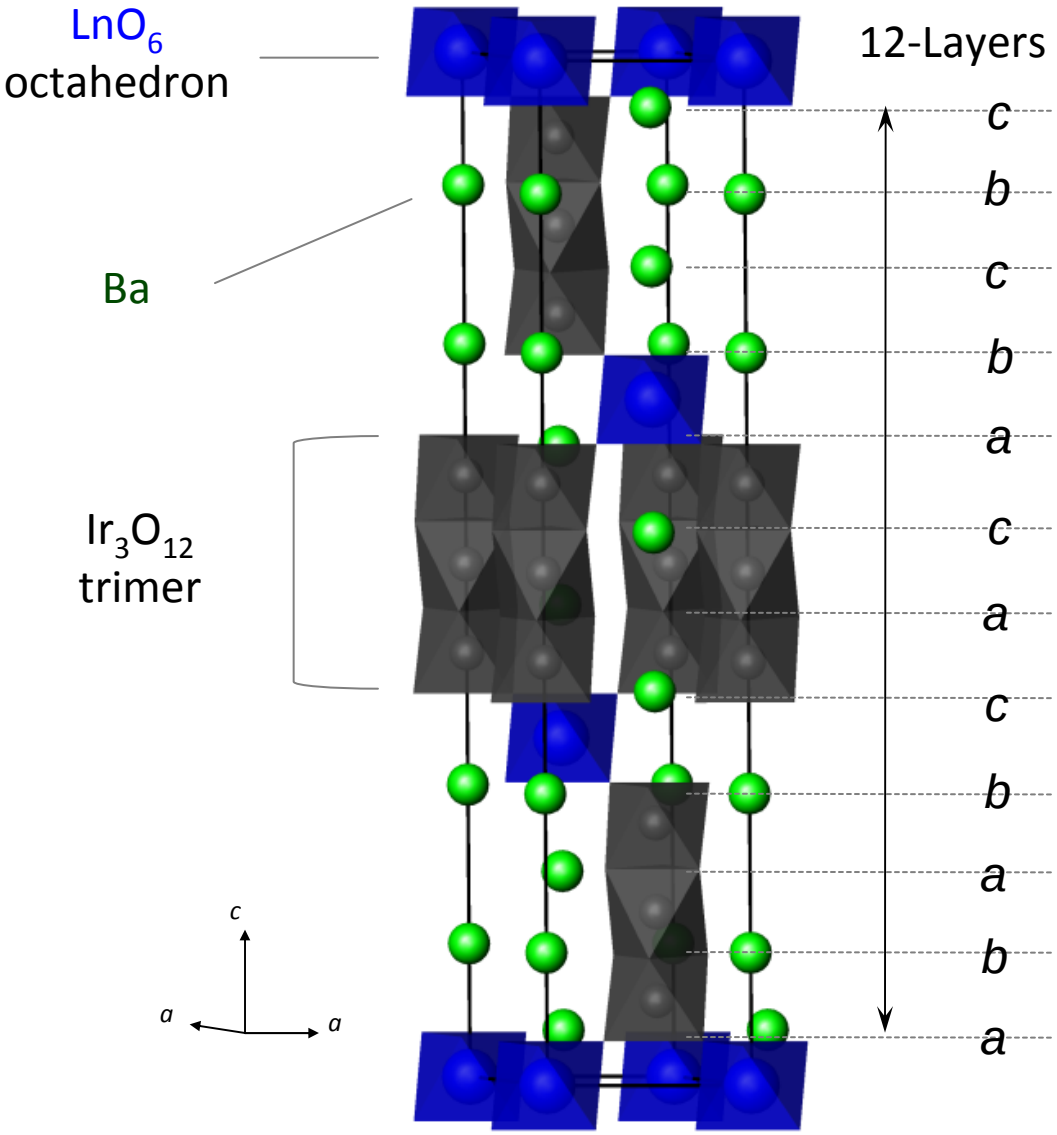
LnO6
octahedron
Ba
Ir3O12
trimer
12-Layers
c
b
c
b
a
c
a
c
b
a
b
a
c
a
a

Fig.2

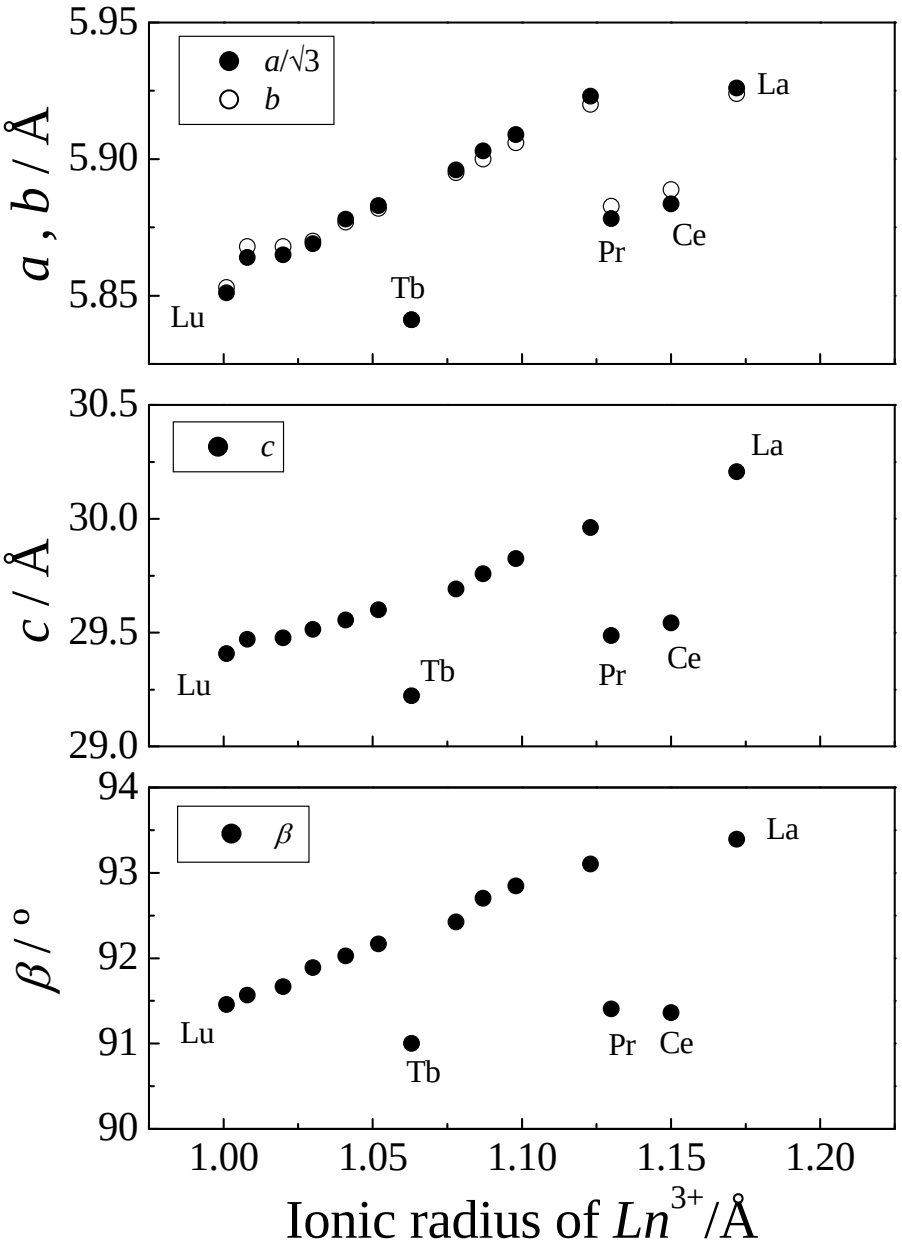
5.95
5.90
5.85
a , b / Å
a/√3
b
La
Ce
Pr
Tb
Lu
30.5
30.0
29.5
29.0
c / Å
c
La
Ce
Pr
Tb
Lu
94
93
92
91
90
β / °
β
La
Pr
Ce
Tb
Lu
1.00
1.05
1.10
1.15
1.20
Ionic radius of Ln3+/Å

Fig.3

(a)

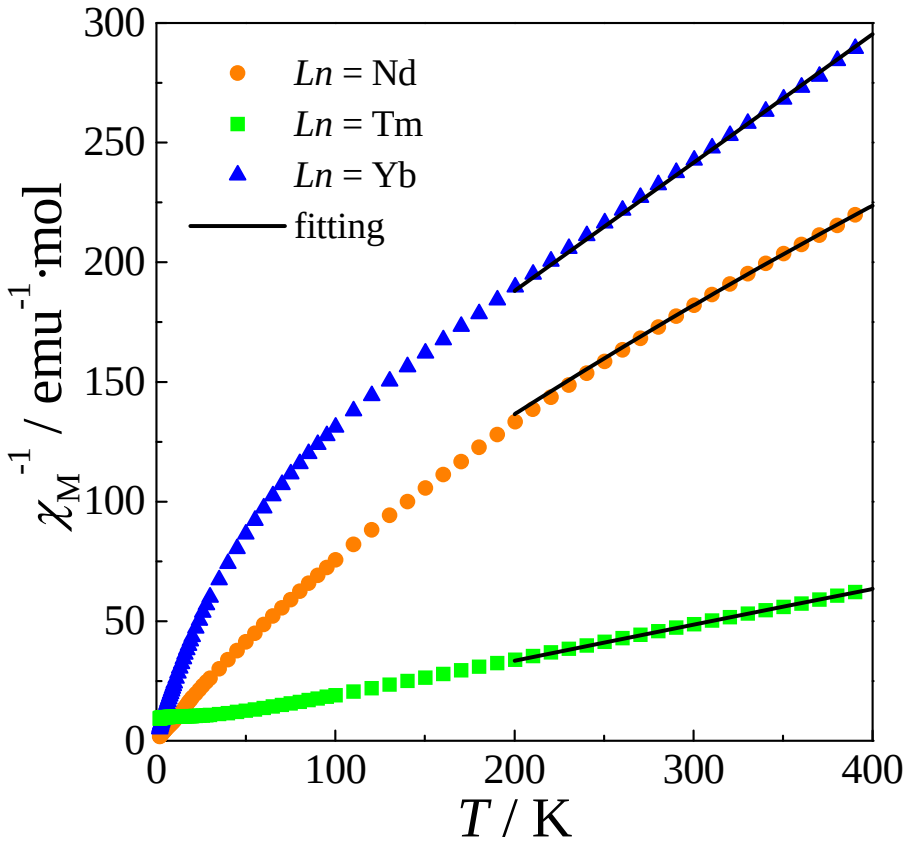
Ln = Nd
Ln = Tm
Ln = Yb
fitting
χM-1 / emu-1·mol
T / K
0
50
100
150
200
250
300
0
100
200
300
400

(b)

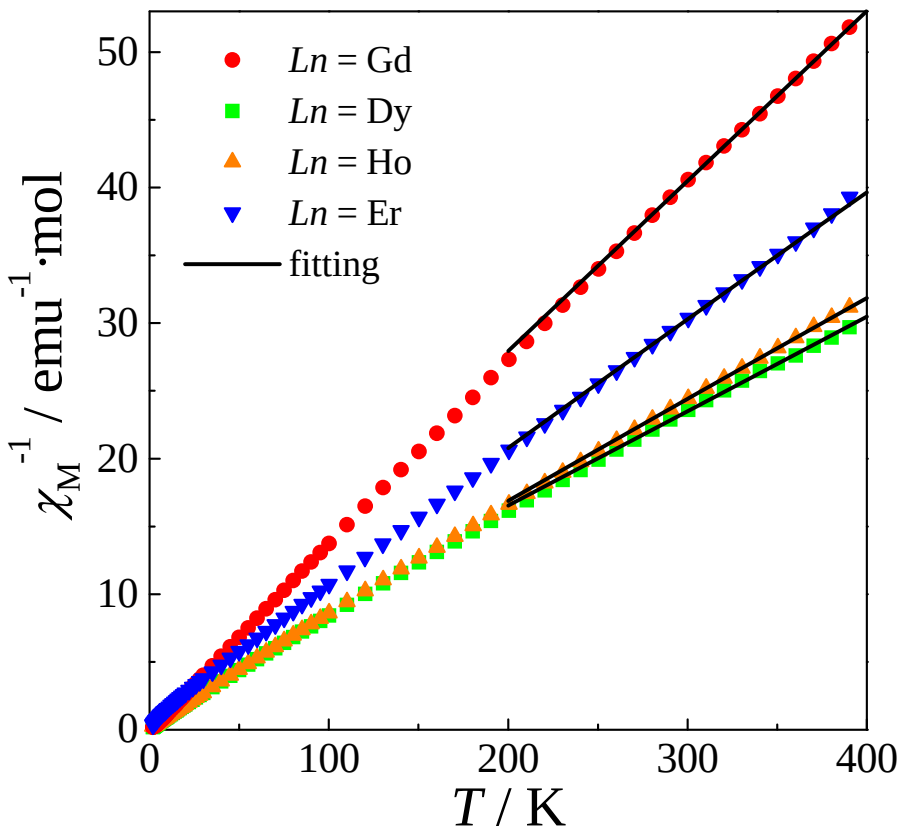
Ln = Gd
Ln = Dy
Ln = Ho
Ln = Er
fitting
χM-1 / emu-1·mol
T / K
0
10
20
30
40
50
0
100
200
300
400

Fig.4

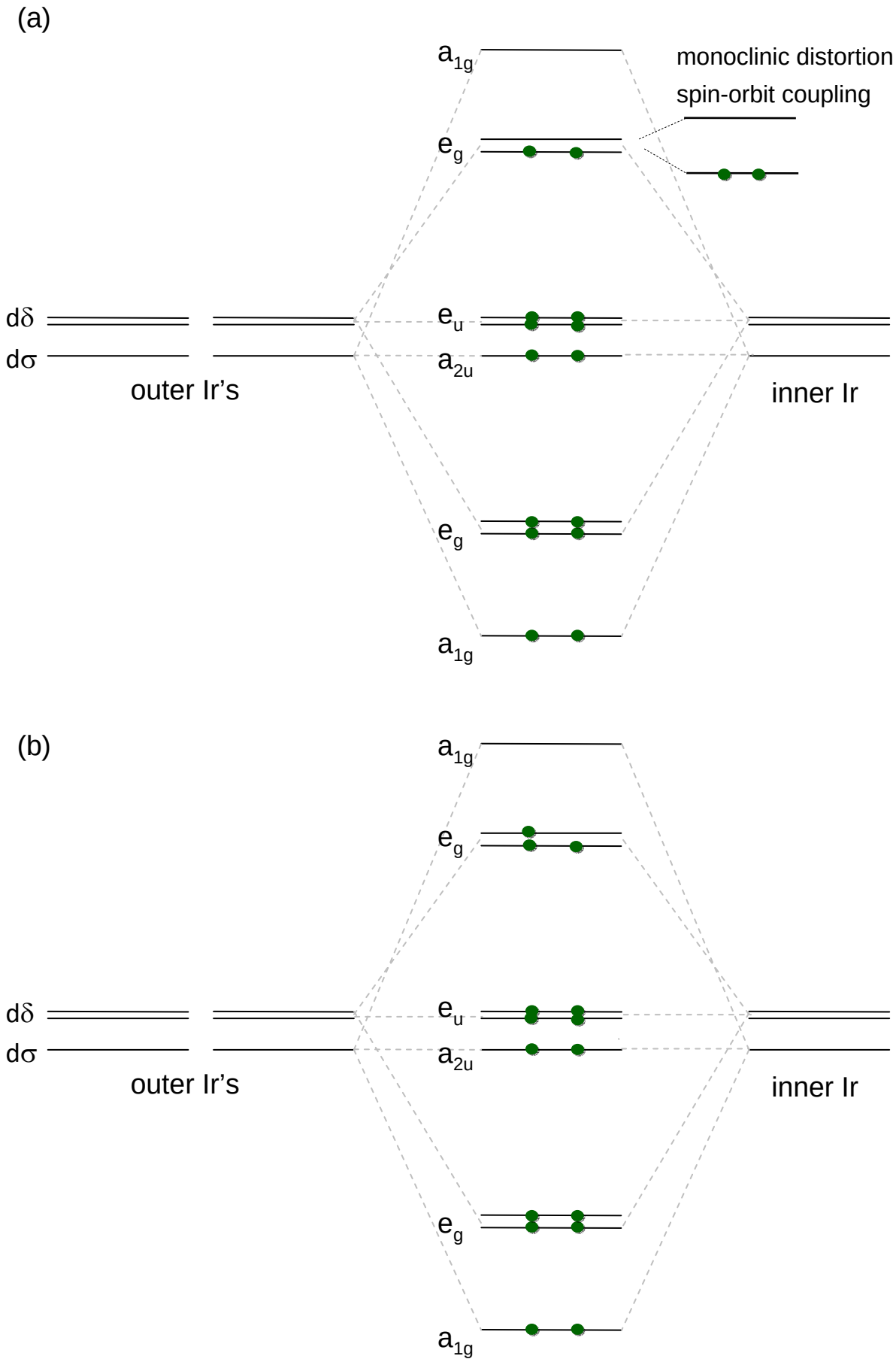
(a)
a1g
monoclinic distortion
spin-orbit coupling
eg
eu
a2u
dδ
dσ
outer Ir's
inner Ir
eg
a1g
(b)
a1g
eg
eu
a2u
dδ
dσ
outer Ir's
inner Ir
eg
a1g

Fig. 5

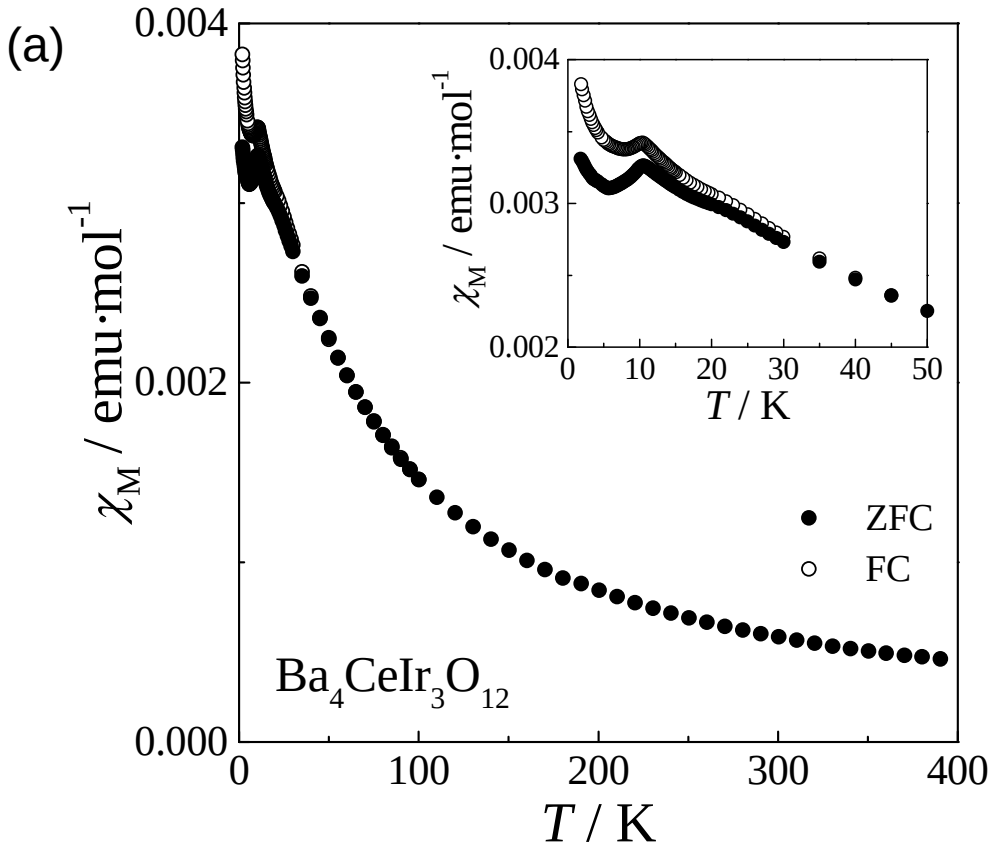
(a)
0.004
0.002
0.000
0
100
200
300
400
χ_M / emu·mol^{-1}
T / K
ZFC
FC
$Ba_4CeIr_3O_{12}$
0.004
0.003
0.002
0
10
20
30
40
50
χ_M / emu·mol^{-1}
T / K

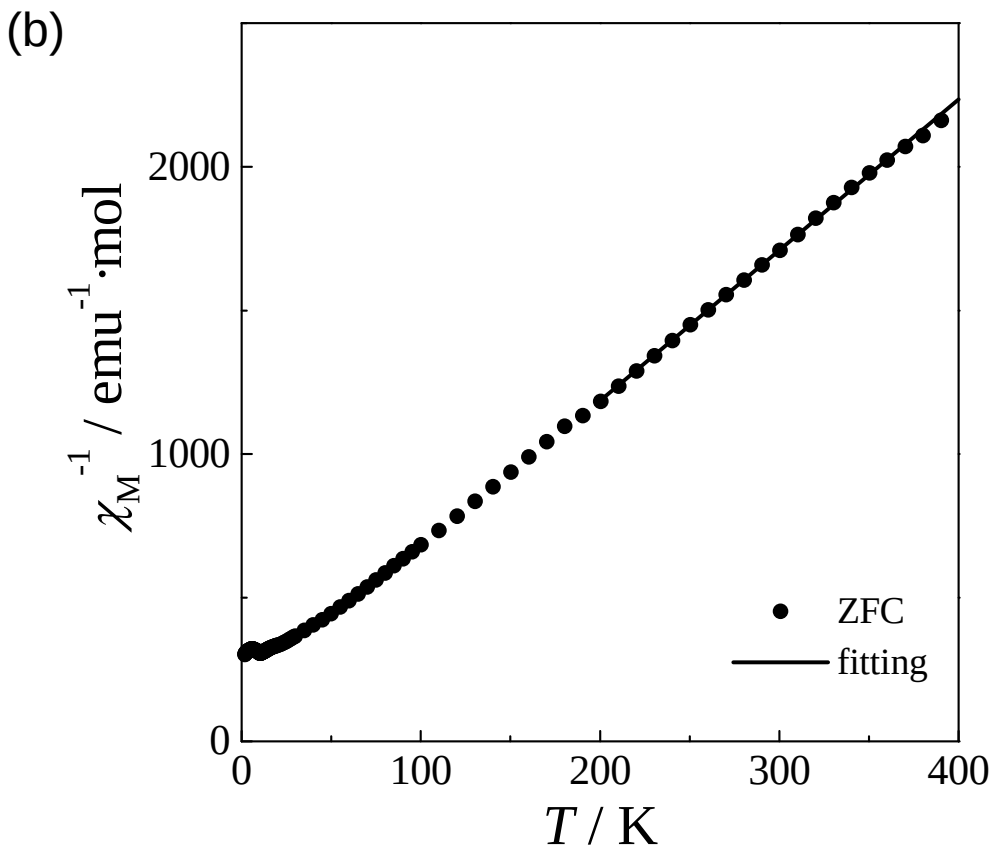
(b)
2000
1000
0
0
100
200
300
400
χ_M^{-1} / emu^{-1}·mol
T / K
ZFC
fitting

Fig.6

(a)

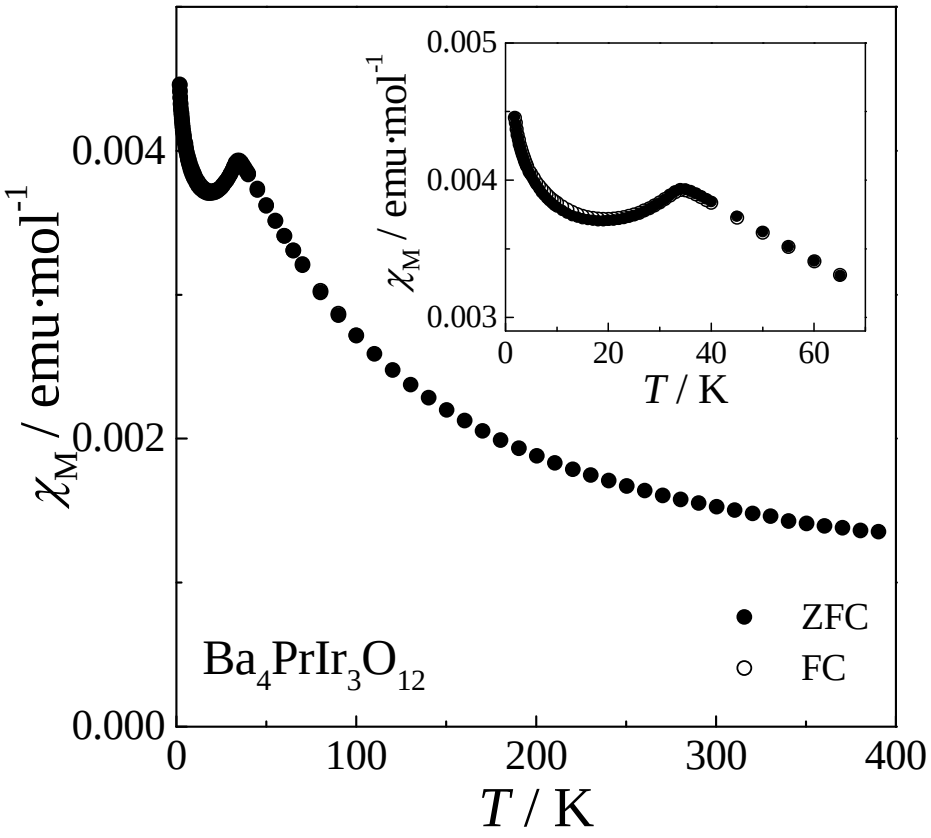
0.004
0.002
0.000
0
100
200
300
400
χ_M / emu·mol^{-1}
T / K
$Ba_4PrIr_3O_{12}$
ZFC
FC
0.005
0.004
0.003
0
20
40
60
χ_M / emu·mol^{-1}
T / K

(b)

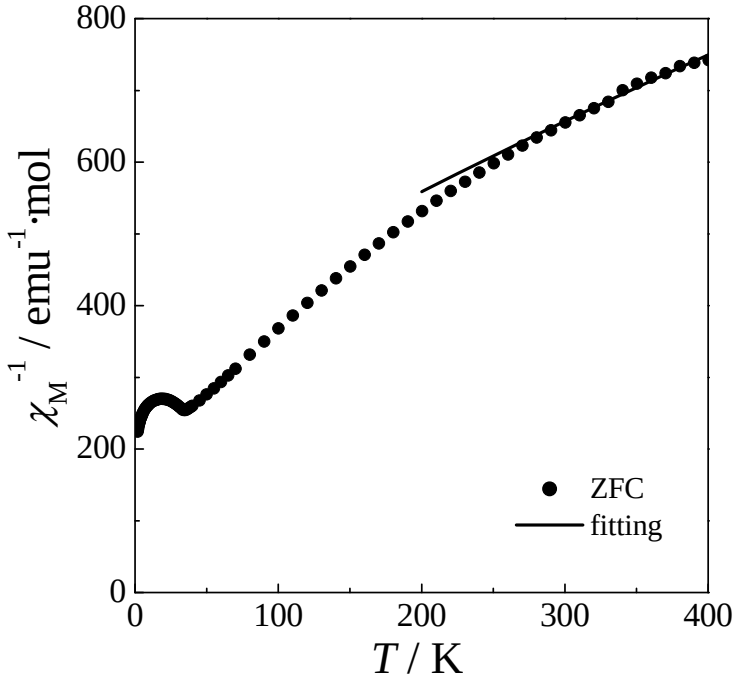
800
600
400
200
0
0
100
200
300
400
χ_M^{-1} / emu^{-1}·mol
T / K
ZFC
fitting

Fig.7

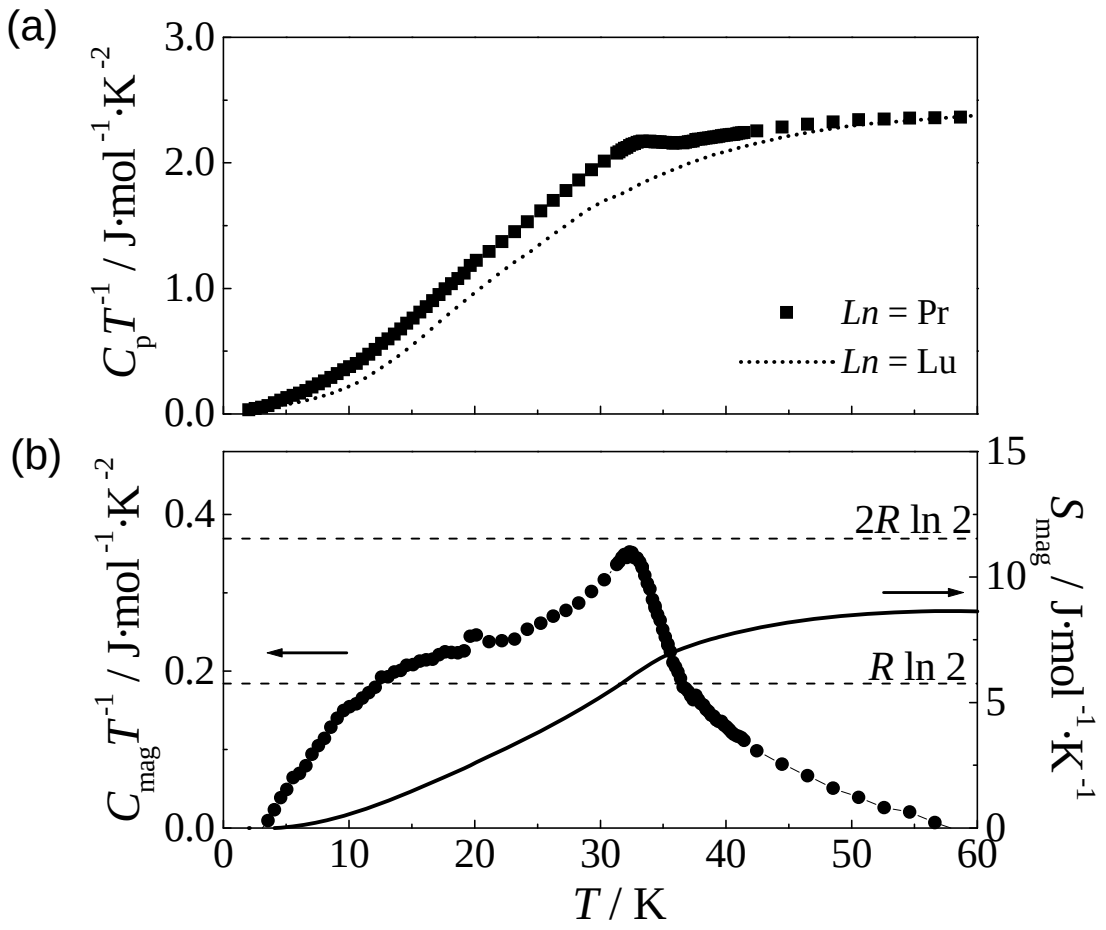
(a)
3.0
2.0
1.0
0.0
C_pT^{-1} / J·mol^{-1}·K^{-2}
Ln = Pr
Ln = Lu
(b)
0.4
0.2
0.0
$C_{mag}T^{-1}$ / J·mol^{-1}·K^{-2}
2R ln 2
R ln 2
15
10
5
0
S_{mag} / J·mol^{-1}·K^{-1}
0
10
20
30
40
50
60
T / K

Fig. 8

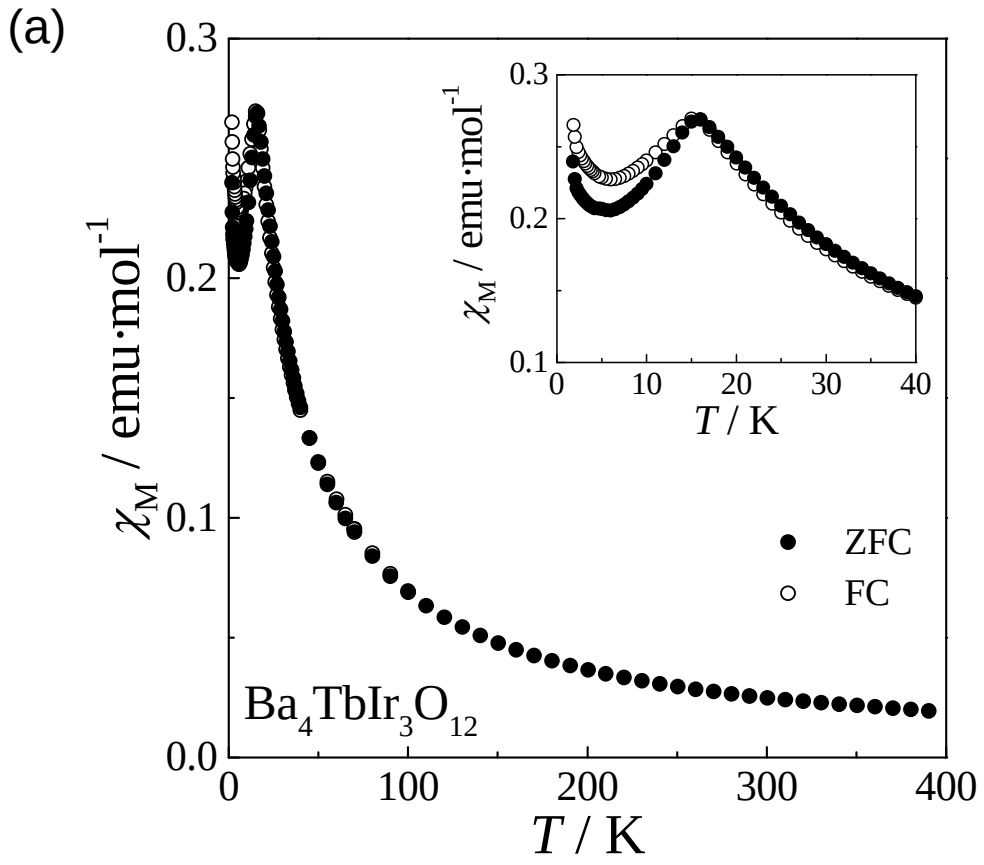
(a)
0.3
0.2
0.1
0.0
χ_M / emu·mol^{-1}
0
100
200
300
400
T / K
ZFC
FC
$Ba_4TbIr_3O_{12}$
0.3
0.2
0.1
χ_M / emu·mol^{-1}
0
10
20
30
40
T / K

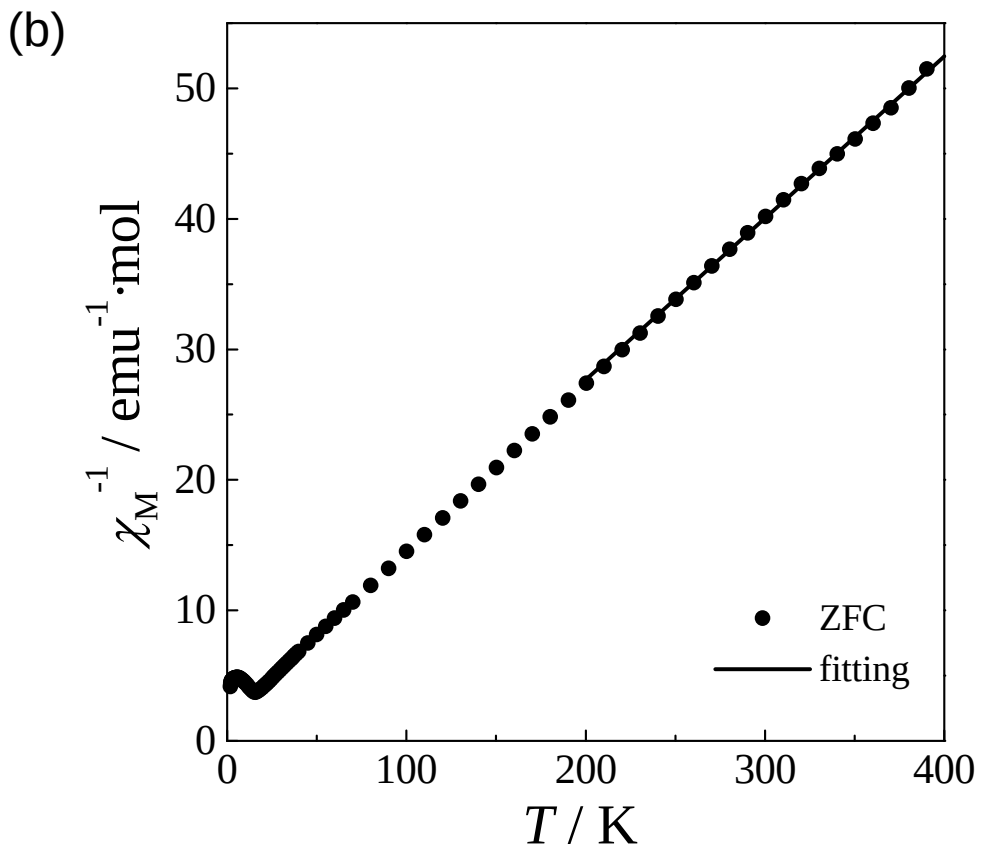
(b)
50
40
30
20
10
0
χ_M^{-1} / emu^{-1}·mol
0
100
200
300
400
T / K
ZFC
fitting

Fig.9

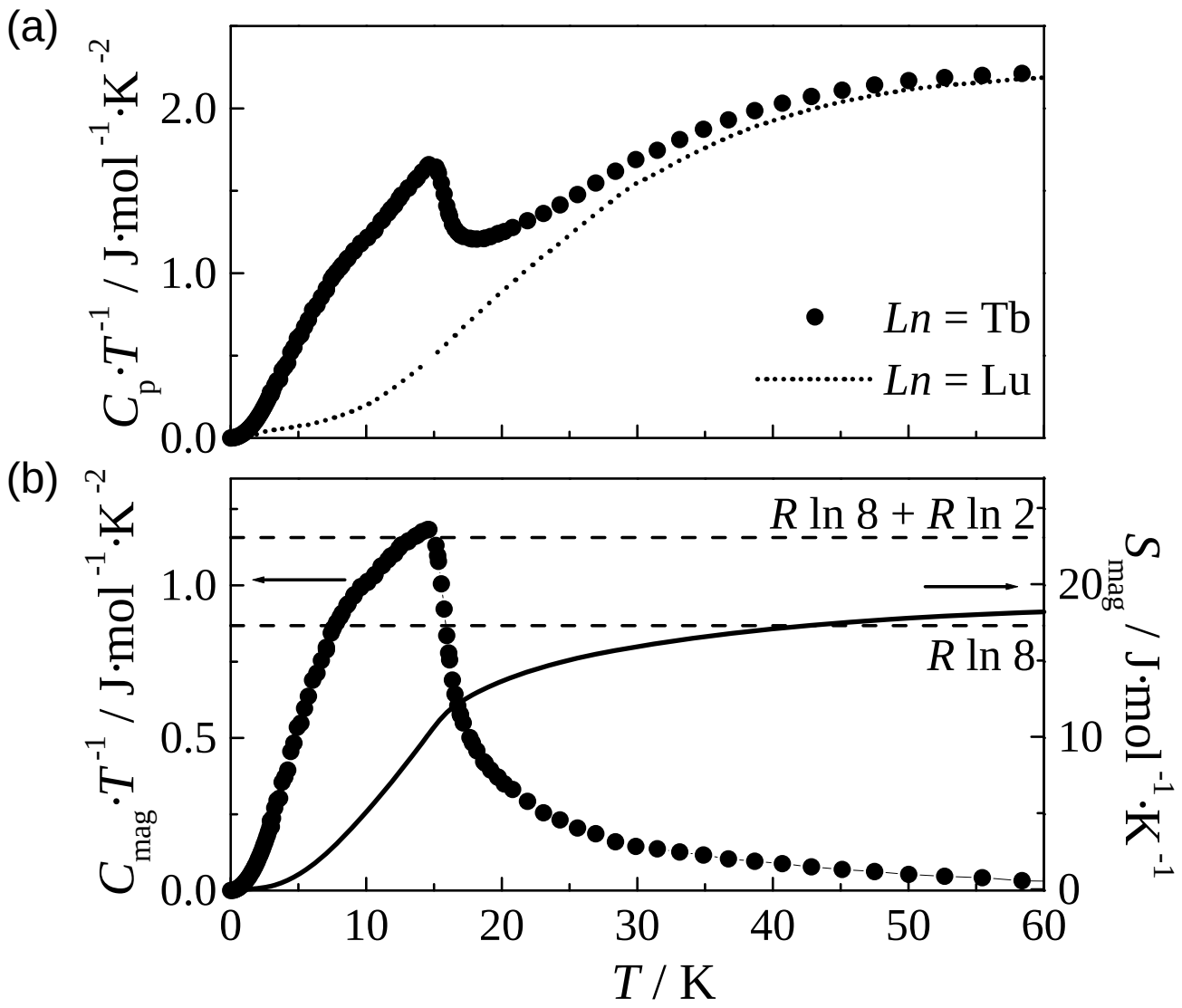
(a)
$C_p \cdot T^{-1}$ / J·mol^{-1}·K^{-2}
2.0
1.0
0.0
Ln = Tb
Ln = Lu
(b)
$C_{mag} \cdot T^{-1}$ / J·mol^{-1}·K^{-2}
R ln 8 + R ln 2
R ln 8
1.0
0.5
0.0
S_{mag} / J·mol^{-1}·K^{-1}
20
10
0
0
10
20
30
40
50
60
T / K

Fig.10

Table 1. Magnetic properties for $Ba_4LnIr_3O_{12}$

Ln^{3+}	electronic configuration	J	μ_{eff} /μ_B	μ_{Ln} [a]/μ_B	magnetic properties
La^{3+}	$4f^0$	0	—	—	diamagnetic
Nd^{3+}	$4f^3$	9/2	3.60	3.62	Curie-Weiss
Sm^{3+}	$4f^5$	5/2		0.84	van Vleck
Eu^{3+}	$4f^6$	0	—	—	van Vleck
Gd^{3+}	$4f^7$	7/2	7.98	7.94	Curie-Weiss
Dy^{3+}	$4f^9$	15/2	10.71	10.63	Curie-Weiss
Ho^{3+}	$4f^{10}$	8	10.36	10.60	Curie-Weiss
Er^{3+}	$4f^{11}$	15/2	9.21	9.59	Curie-Weiss
Tm^{3+}	$4f^{12}$	6	7.31	7.57	Curie-Weiss
Yb^{3+}	$4f^{13}$	7/2	3.86	4.54	Curie-Weiss
Lu^{3+}	$4f^{14}$	0	—	—	diamagnetic

Ln^{4+}	electronic configuration	J	μ_{eff} /μ_B	μ_{cal} [b]/μ_B	magnetic properties (T_N)
Ce^{4+}	$4f^0$	0	1.61	1.73	antiferromagnetic (10.5 K)
Pr^{4+}	$4f^1$	5/2	2.94	3.07	antiferromagnetic (35 K)
Tb^{4+}	$4f^7$	7/2	8.02	8.13	antiferromagnetic (16 K)

a μ_{Ln}: free ion values for Ln^{3+}.

b μ_{cal}: calculated moments for Ln^{4+} and S = 1/2 (see text).